(Received 6 June 2023, Accepted 30 April 2024, Scheduled 4 May 2024)

Multi-Characteristic Integrated Ultra-Wideband Frequency Selective Rasorber

Dengpan Wang[1,4], Xingshuo Cui[1,4], Dan Liu[3,4], Xiaojun Zou[2,*], Guangming Wang[1,*], Bin Zheng[3], and Tong Cai[1,*]

[1]*Air and Missile Defense College, Air Force Engineering University, Xi'an 710051, China*
[2]*College of Information and Communication, National University of Defense Technology, Wuhan 430035, China*
[3]*State Key Laboratory of Modern Optical Instrumentation The Electromagnetics Academy Zhejiang University, Hangzhou 310027, China*
[4]*These authors contributed equally*

ABSTRACT: Frequency selective rasorbers (FSRs), especially those with ultra-wideband and hybrid characteristics, are of great significance in modern stealth technology and applications. However, currently available FSRs have issues with limited transmission bandwidth and single operating characteristics. Here, a novel strategy is proposed to design multi-characteristic integrated FSRs with ultra-wide and high-efficiency passband via spoof surface plasmon polariton (SSPP). The designed FSR exhibits the characteristics of absorption-transmission (AT), transmission-absorption (TA), and absorption-transmission-absorption (ATA), which consists of AT resistive sheets, TA SSPP slow-wave structures, and ultra-wideband bandpass frequency selective surface (FSS). The top lumped-resistor-loaded resistive sheet and the bottom multi-layer cascaded FSS form an AT FSR which is demonstrated by equivalent circuit model (ECM). Middle dispersion gradient SSPP structure that generates SSPP on the periodic array is an independent TA FSR while the working principle is based on k-dispersion control and energy distribution. Thus, the transition band between the transmissive and absorptive bands is narrowed while the crosstalk between absorber and transmission is avoided. For verification, a prototype is fabricated and experimentally demonstrated. Measured results manifest the validity and feasibility of the FSR with an ultra-wide -1 dB transmission band from 8.9 to 16.4 GHz (59.3%) and two 85% absorption bands covering 2.2–6.4 GHz (97.7%) and 17.6–26 GHz (38.5%). Our work provides a novel method for the design of an ultra-wideband multi-characteristic FSR and stimulates its application in broadband electromagnetic stealth, shielding and compatible devices.

1. INTRODUCTION

Frequency selective rasorbers (FSRs), which can transmit in-band electromagnetic (EM) waves with low insertion loss and perfectly absorb out-of-band energy for radar cross section (RCS) reduction, exhibit great application prospects and urgent needs in fields such as stealth antennas, radomes, and wireless communication systems [1–9]. Consequently, numerous FSRs with excellent performance and various requirements have been reported in recent years [10–16]. According to the relative location of the transmission and absorption bands, current available FSRs can be classified into three categories, including absorption-transmission (AT) [17–20], transmission-absorption (TA) [21–24], and absorption-transmission-absorption (ATA) [25–31]. FFollowing the broadband trend of modern EM stealth, shielding and compatible systems, dual-polarized ATA FSRs with ultra-wide and high-transmission passband are of great interest and expectation due to their safest and most practical EM transparent windows. Nevertheless, such FSRs are more difficult to achieve since the transition band between transmission and absorption bands suffers from the issues of high insertion loss, limited passband bandwidth, and narrow absorption band [5, 10, 25, 31].

Recently, many efforts have been made to address these issues. Structures with multi-mode resonators have been widely used in the design of 2D FSRs and meta-devices with wide and nearly transparent windows, such as circular spiral resonator, convoluted resonator, and multiple coplanar parallel resonator [32–34, 57, 58]. The relative bandwidths of these 2D FSRs can reach about 30% with broad absorption. To further expand the passband bandwidth, a 2.5D ATA FSR with a relative bandwidth (-1 dB passband) of 40.5% is proposed, but the two absorption bands are narrow [35, 36]. In addition, some researchers have introduced 3D FSRs based on parallel waveguides and planar slot lines to obtain better performance, achieving a relative bandwidth of 40% of -1 dB passband and two wide absorption bands [37–39]. Despite these achievements, the passband of the existing ATA FSR is still narrow compared to the operating bandwidth of modern ultra-wideband radar and wireless communication systems. On one hand, most methods of expanding the passband bandwidth rely on multi-mode resonances within the passband, which inherently limits its bandwidth. On the other hand, most ATA FSRs are designed as a whole structure, so they face the challenge of mutual interfer-

* Corresponding authors: Tong Cai (caitong326@sina.cn); Xiaojun Zou (zouxj0606@163.com); Guangming Wang (wgming01@sina.com).

ence from the transmission and absorption bands and are limited to a single operational characteristic.

Fortunately, due to the properties of sub-wavelength resolution and local field enhancement, spoof surface plasmon polariton (SSPP) shows efficient transmissive characteristic below the cut-off frequency and strong reflection above the cut-off frequency, which provides an alternative and flexible efficient path for designing transmission line, filter, rejector, and FSS [40–45]. Moreover, wideband EM absorbers based on SSPP have been proposed for RCS reduction, which have wide angular stabilities for both transverse electric waves and transverse magnetic waves [46–48]. The excellent performance of SSPP in above applications makes it a new candidate for FSR design.

In this paper, we propose a novel guideline and technique protocol to implement a multi-characteristic integrated ATA FSR with ultra-wide transparent window between two road absorption bands through combining the FSS and SSPP advantages. The complete ATA FSR consists of two independent subsets, namely AT FSR and TA FSR. The AT FSR consists of an AT resistive sheet and an ultra-wide bandpass FSS, which are separated by an air layer. Moreover, the planar periodic SSPP slow-wave structure is equivalent to TA FSR, which effectively transmits SSPP below the cut-off frequency and strongly absorbs energy above the cut-off frequency. The overlap of the passband in ultra-wide bandpass FSS and the planar periodic SSPP slow-wave structure is used to expanding the passband bandwidth. The final ATA FSR can be easily achieved by replacing the air gap in the AT FSR with a TA SSPP structure to construct a compact design without additional profile, as shown in Fig. 1. Simulated results are in good accordance with the measured ones, indicating that the 1 dB relative bandwidth of the passband can reach 59.3% with two wide absorption bands. Among the above process, the equivalent circuit model (ECM) and dispersion control engineering are investigated and analyzed for the FSR design. Specially, the transition band between the transmissive and absorptive bands is narrowed while the crosstalk between absorber and transmission is avoided. The proposed multi-characteristic integrated FSR has enormous applications in ultra-wideband stealth antennas, radomes, and other EM compatibility devices.

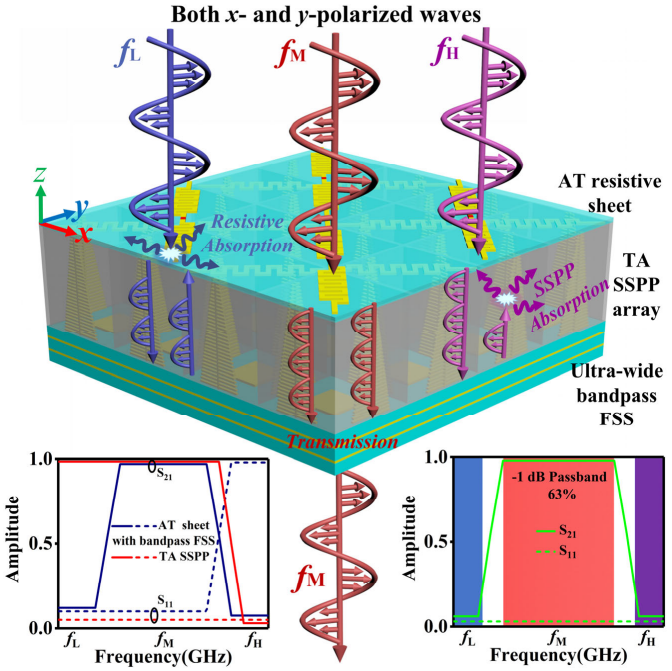

FIGURE 1. Schematic and operating mechanism of the ultra-wide multi-characteristic ATA FSR. When x- and y-polarized EM waves are irradiated on the FSR, the absorption occurs in the low-frequency band f_L and high-frequency band f_H, caused by the ohmic loss of the resistive sheet and the material loss of the SSPP array, respectively. Meanwhile, an ultra-wide nearly transparent window occurs in the middle-frequency band f_M. The insets are the theoretical EM responses of the AT, TA, and complete ATA FSR meta-atom.

2. OPERATING MECHANISM AND DESIGN GUIDELINE OF THE ATA FSR

Figure 2(a) depicts the schematic of the designed FSR meta-atom consisting of an AT resistive sheet and a 2×2 bandpass FSS super-cell, between which is a 2×2 TA SSPP array. The upper AT resistive sheet is implemented by two orthogonal lumped-resistor-loaded cross-dipoles with miniaturized zigzag lines on both sides of a Rogers substrate, as shown in Fig. 2(c). Fig. 2(d) displays that each unit cell of the bandpass FSS super-cell is composed of two square resonators and two coupling square slots. As for that of the TA SSPP array in Fig. 2(b), four metallic blade arrays with a dispersion gradient are symmetrically attached to the FR-4 substrates. Here, the upper resistive sheet and bottom bandpass FSS construct an AT FSR, while the middle TA SSPP array is a TA FSR, which together forms an ATA FSR. It is worth noting that all the structures are symmetrically designed to achieve polarization insensitivity. For simplicity and generality, an x-polarized plane wave (the wave vector is in the $-z$ direction, and the electric field is parallel to the x direction) is adopted in this paper to analyze the design and mechanism of all dual-polarized structures. In this part, we first adopt ECM for the design and analysis of AT resistive FSR, then analyze the working principle of TA SSPP FSR based on k-dispersion control and energy distribution. Finally, the complete ATA FSR with ultra-wideband transmission performance between two wide absorption bands is implemented and examined.

2.1. Design and Analysis of AT FSR Meta-Atom Based on ECM

The AT FSR meta-atom performs excellent absorption ability in the low band and an ultra-wide high-efficiency transmission performance in the middle and high bands. Absorption is generated by the ohmic loss on the resistive sheet with the assistance from the out-of-band ground effect of the FSS, while the ultra-wide transparent window is formed by the efficient transmission performance of both the resistive sheet and FSS in the middle and high bands. We first design a dual-polarized AT resistive sheet with two orthogonal cross-dipoles placed at an angle of 45° on both sides of the Rogers substrate. Each cross-dipole is composed of miniaturized zigzag lines to generate strong resonance at low frequencies, while an optimized lumped resistor

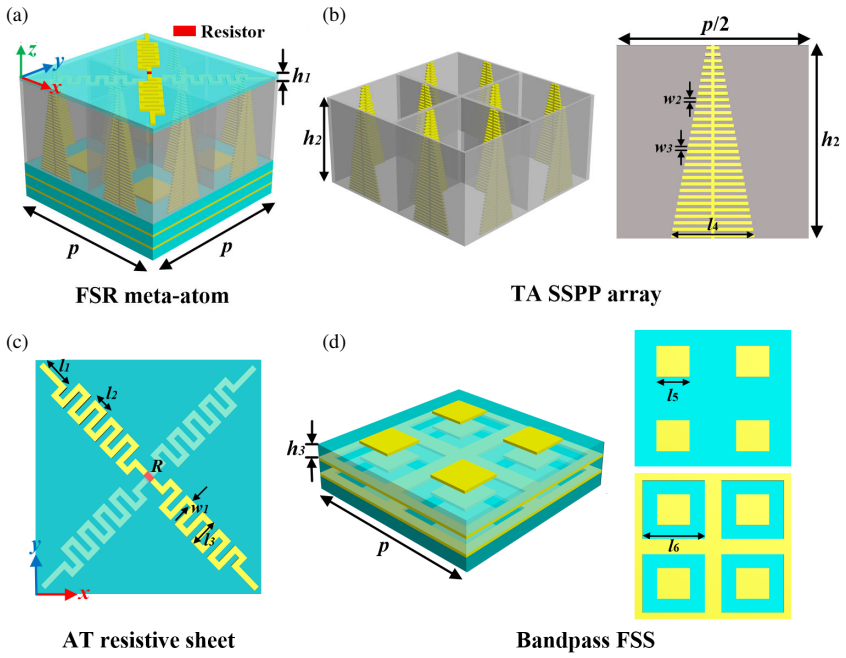

FIGURE 2. The configuration and geometric parameters of the proposed multi-characteristic ATA FSR. (a) The complete ATA FSR meta-atom. (b) The dispersion-gradient TA SSPP metallic blade array. (c) The lumped-resistor-loaded AT resistive sheet. (d) The four-layer cascaded bandpass FSS super-cell. The specific geometric parameters are as follows: $p = 24\,\text{mm}$, $h_1 = 0.508\,\text{mm}$, $h_2 = 12\,\text{mm}$, $h_3 = 2\,\text{mm}$, $w_1 = 0.5\,\text{mm}$, $w_2 = w_3 = 0.2\,\text{mm}$, $l_1 = 4\,\text{mm}$, $l_2 = 1.7\,\text{mm}$, $l_3 = 2.8\,\text{mm}$, $l_4 = 5.2\,\text{mm}$, $l_5 = 5.1\,\text{mm}$, $l_6 = 9.3\,\text{mm}$.

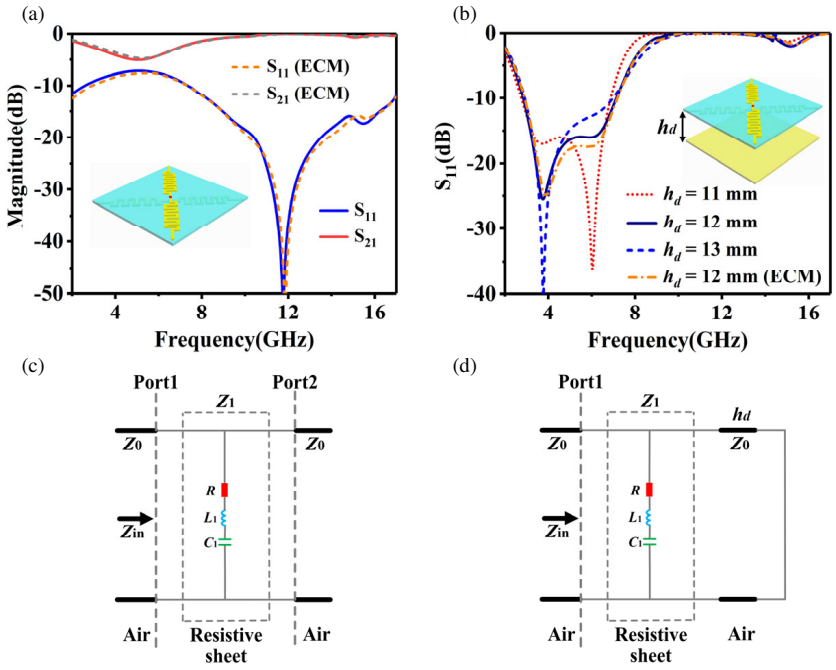

FIGURE 3. The design verification and ECM analysis of the resistive sheet. (a) The EM response of the resistive sheet calculated by the ECM and CST. (b) The EM response of the resistive sheet with a metal plane at different distances h_d, calculated by the ECM and CST. (c) The ECM of the resistive sheet. (d) The ECM of the resistive sheet with a metal plane.

is mounted at the center of the zigzag lines to absorb energy. Fig. 3(a) shows the simulated transmission and reflection magnitudes of the designed AT resistive sheet. It is observed that an absorption effect appears at low frequencies, and an ultra-wide -1 dB passband starting from 8.3 GHz is achieved. Moreover, a metallic plane is placed at a distance h_d below the resistive sheet to study the low-band absorption performance [32]. The ideal absorber displays a perfect absorption effect with two resonances, and the distance h_d determines the resonance frequency and absorption effect, as plotted in Fig. 3(b). To bet-

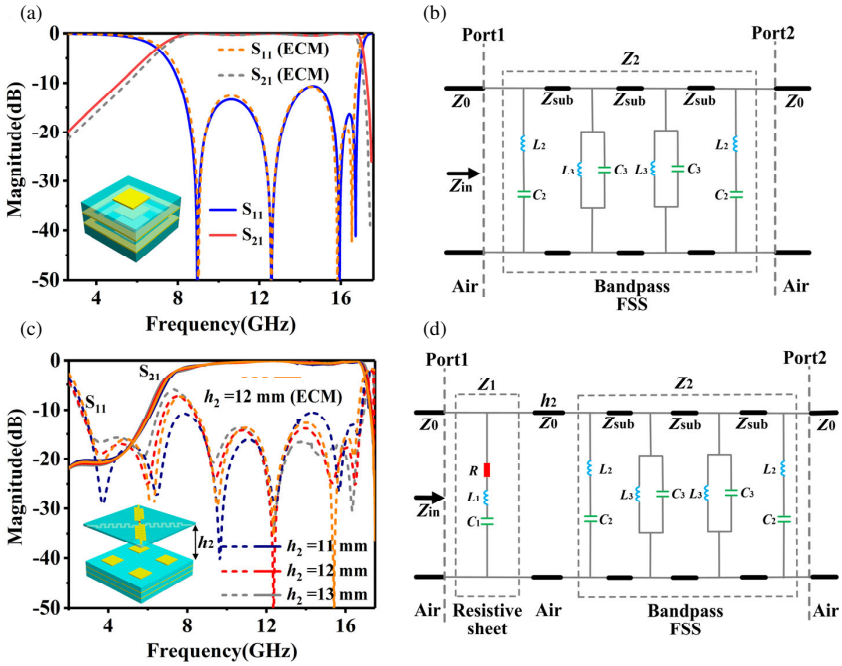

FIGURE 4. The design verification and ECM analysis of the bandpass FSS and AT FSR. (a) The EM response of the bandpass FSS calculated by the ECM and CST. (b) The ECM of the bandpass FSS. (c) The EM response of the AT FSR with an air gap at different distances h, calculated by the ECM and CST. (d) The ECM of the AT FSR. Here, $L_2 = 2.58\,\text{nH}$, $C_2 = 0.03\,\text{pF}$, $L_3 = 0.38\,\text{nH}$, and $C_3 = 0.42\,\text{pF}$.

ter understand the operation mechanism of the resistive sheet, the ECM is presented and analyzed for the resistive sheet design, as illustrated in Figs. 3(c) and (d). Here, the resistive sheet composed of two lumped-resistor-loaded cross-dipoles is equivalent to a series RLC circuit, since the cross-dipole with miniaturized zigzag lines is equivalent to a series LC circuit [49]. The equivalent inductor L and capacitor C, which can be calculated by dimensions of the cross-dipoles [50], determine the absorption frequency (i.e., resonant frequency), while the optimized lumped resistor R determines the absorption effect. Perfect absorption can be obtained when the impedance of the resistive sheet with a metal plane matches the air characteristic impedance. After optimizing values as $R = 250\,\Omega$, $L_1 = 10.1\,\text{nH}$, and $C_1 = 0.11\,\text{pF}$, the ECM is constructed to analyze and verify. The EM responses calculated by the above ECM are shown in Figs. 3(a) and (b), which are in good agreement with the numerical simulation results by CST.

Meanwhile, a dual-polarized FSS with an ultra-wide passband is necessary for the AT FSR design, as depicted in Fig. 2(d). The designed FSS is composed of a four-layer cascaded structure to achieve ultra-wide and high-transmission passband, with two square metallic patches mounted on the top and bottom substrates, and two square coupling slots printed on the two substrates in the middle layer. In this design, the square metallic patches of the top and bottom layers are the same, and the square coupling slots of the middle two layers are also the same. The entire FSS structure is similar to the resonator-coupler-coupler-resonator model, and four transmission poles can be excited, resulting in a four-order ultra-wideband bandpass response, as presented in Fig. 4(a). Moreover, the ECM of the bandpass FSS is depicted in Fig. 4(b), which consists of two series LC circuits and two parallel LC circuits. The square metallic patches are equivalent to series LC circuits, and the square coupling slots are equivalent to parallel LC circuits [51, 52]. Such an ECM can generate four parallel resonances, where the equivalent impedance Z_2 of FSS is infinite, and an ultra-wide passband can be obtained. The simulation results, which are in good agreement with ECM analysis, indicate that the designed FSS exhibits an ultra-wide $-1\,\text{dB}$ passband from 7.6 to 17 GHz (76.4%) and a strong reflection in the low band, as shown in Fig. 4(a).

With the EM responses and ECMs of the resistive sheet and bandpass FSS, an AT FSR meta-atom is designed, and its operating mechanism is analyzed. The AT FSR is constructed by replacing the metal plane below the resistive sheet with the designed bandpass FSS, as depicted in Fig. 4(c). In the low absorption band from 2.3 to 6.4 GHz, the FSS with strong reflection can be regarded as a metal plane, and the combination of the resistive sheet and ground FSS will produce perfect absorption. As for the middle and high transmission bands from 7.8 to 16.9 GHz, an ultra-wide transparent window with 1 dB insertion loss is obtained. Meanwhile, the air gap between the resistive sheet and FSS has a significant impact on low-frequency absorption performance, as it constitutes the equivalent impedance of AT FSR, and the conclusion is similar to the ideal absorber in Fig. 3(b). Moreover, with the help of resistive sheet and bandpass FSS ECMs mentioned above, we adopt a complete ECM to analyze the operating mechanism and guide the universal design for FSR, as displayed in Fig. 4(d). Here, Z_1, Z_0, and Z_2 represent the impedances of resistive sheet, air, and bandpass FSS, respectively. According to transmission line

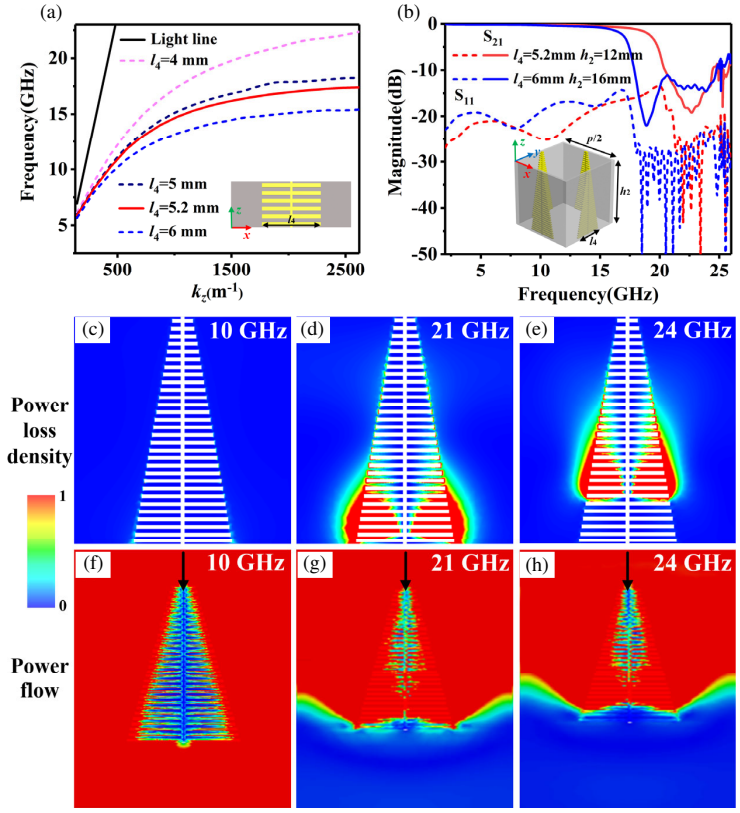

FIGURE 5. The design and analysis of the TA FSR with dispersion gradient SSPP array. (a) Dispersion relations of SSPP metallic blade arrays with different lengths l_4. (b) EM responses of the TA FSR with different dispersion gradient SSPP arrays. (c)–(e) Power loss densities and (f)–(h) power flows of the TA FSR at different frequencies.

theory with *ABCD* and S matrixes, the reflection coefficient S_{11} and transmission coefficient S_{21} of the two-port ECM can be expressed as [5]:

$$S_{11} = \frac{-\frac{Z_0(Z_1+Z_2)}{\tan\theta} + jZ_0\left(Z_1 - Z_0 - Z_2\right)}{j2Z_1Z_2 + \frac{2Z_1Z_2+Z_0(Z_1+Z_2)}{\tan\theta} + jZ_0\left(Z_0 + Z_1 + Z_2\right)} \tag{1}$$

$$S_{21} = \frac{2Z_1Z_2}{\left(2Z_1Z_2 + Z_0(Z_1+Z_2)\right)\cos\theta + \left[2Z_1Z_2 + Z_0\left(Z_0 + Z_1 + Z_2\right)\right] j\sin\theta} \tag{2}$$

where $\theta = \beta h_2 = 2\pi f h_2/c$ represents the propagation phase, β the propagation constant, f the working frequency, and c the speed of light.

In the low absorption band, bandpass FSS is equivalent to a metal plane, whose equivalent impedance Z_2 is 0. Therefore, S_{21} in Equation (2) is 0, and S_{11} in Equation (1) can be written as

$$S_{11} = \frac{-\frac{Z_0Z_1}{\tan\theta} + jZ_0\left(Z_1 - Z_0\right)}{\frac{Z_0Z_1}{\tan\theta} + jZ_0\left(Z_0 + Z_1\right)} \tag{3}$$

Meanwhile, the complete ECM is simplified as the circuit of resistive sheet with a metal plane, as depicted in Fig. 3(d). To achieve perfect absorption, S_{11} in Equation (3) should be equal to 0 with the impedance Z_1 satisfying

$$Z_1 = \frac{Z_0\left(1 - \frac{j}{\tan\theta}\right)}{1 + \frac{1}{\tan^2\theta}} \tag{4}$$

which is the design and optimization guideline for loaded lumped resistor R.

In the middle and high transmission bands, the equivalent impedance Z_2 is infinite due to the parallel resonance. Thus, the complete ECM is simplified as the circuit of resistive sheet without a metal plane by replacing the FSS with an open circuit, as depicted in Fig. 3(c). The impedance Z_1 is infinite from 8.3 GHz in our design of resistive sheet. Therefore, with $Z_1 = Z_2 = \infty$, S_{11} and S_{21} in Equations (1) and (2) become:

$$S_{11} = \frac{Z_{\text{air}}^2 - Z_0^2}{Z_{\text{air}}^2 + Z_0^2} = 0 \tag{5}$$

$$S_{21} = \frac{-j2Z_{\text{air}}Z_0}{Z_{\text{air}}^2 + Z_0^2} = -j \tag{6}$$

It can be seen that a transparent window is generated in the ultra-wide middle to high frequency band, which is well consistent with the design of the resistive sheet. In summary, all ECM analyses are in good agreement with theoretical derivation and simulation design, demonstrating the feasibility and universality of ECM analysis in guiding FSR design.

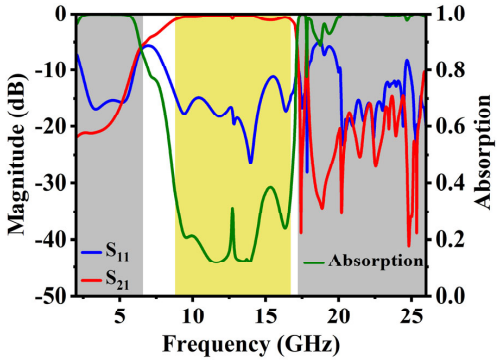

FIGURE 6. The design and EM response of the complete ATA FSR meta-atom.

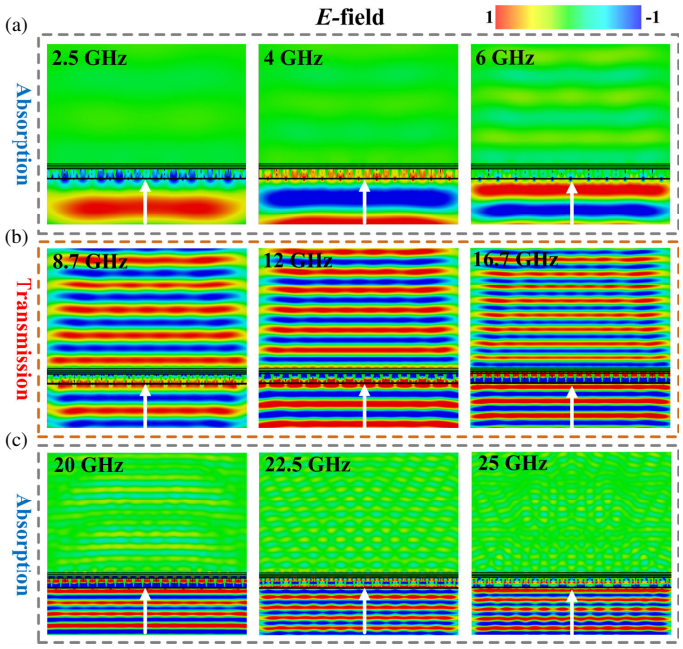

FIGURE 7. Simulated Re(E_x) field patterns of the ATA FSR in the (a) low absorption band with $f_L = 2.5$ GHz, 4 GHz, and 6 GHz, (b) middle transmission band with $f_M = 8.7$ GHz, 12 GHz, and 16.7 GHz, and (c) high absorption band with $f_H = 20$ GHz, 22.5 GHz, and 25 GHz.

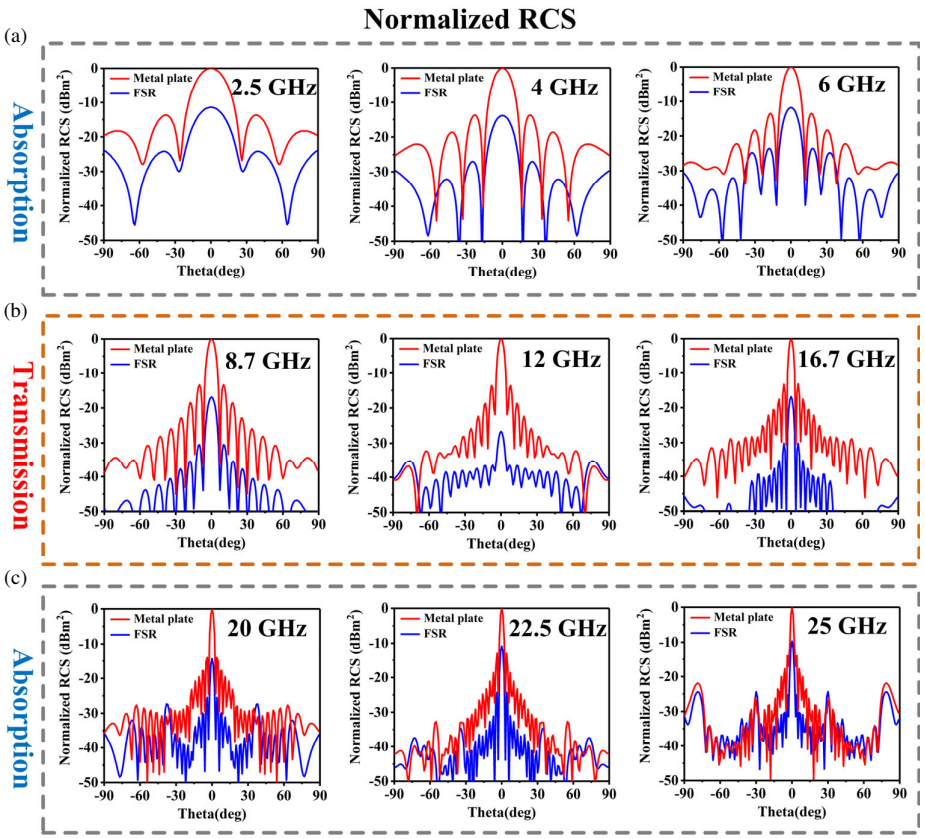

FIGURE 8. Normalized RCS of the ATA FSR and the metal plate in the (a) low absorption band with $f_L = 2.5$ GHz, 4 GHz, and 6 GHz, (b) middle transmission band with $f_M = 8.7$ GHz, 12 GHz, and 16.7 GHz, and (c) high absorption band with $f_H = 20$ GHz, 22.5 GHz, and 25 GHz.

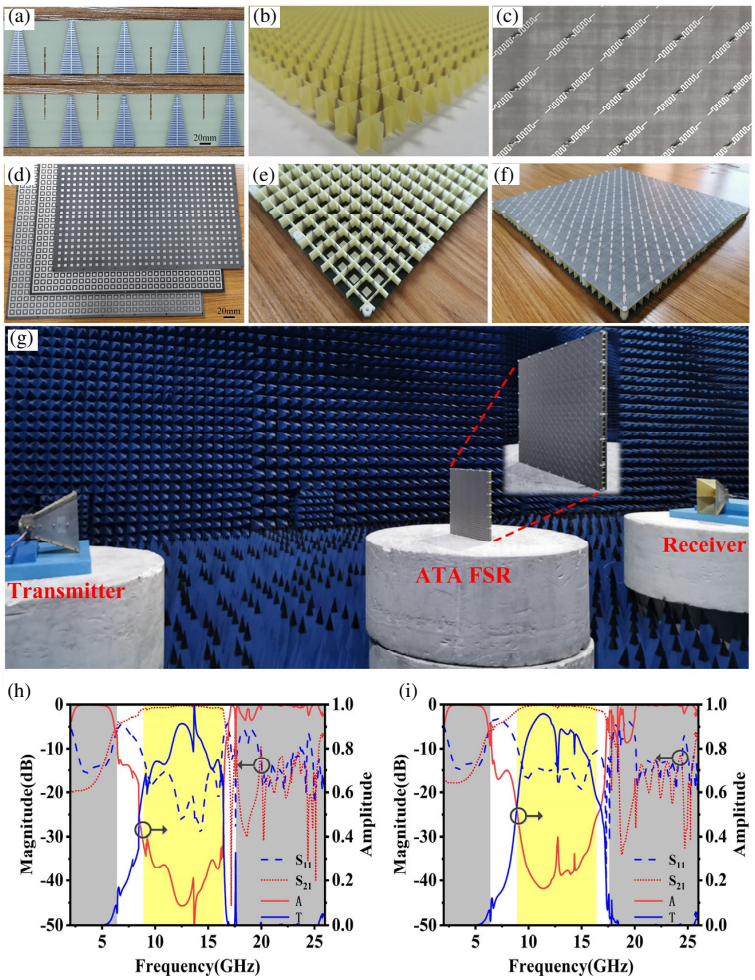

FIGURE 9. Fabricated prototypes and experimental verification of the ATA FSR. Prototypes of the (a) dispersion gradient metallic blade array, (b) TA SSPP array, (c) AT resistive sheet, (d) bandpass FSS, (e) combination of TA SSPP array and bandpass FSS, and (f) complete ATA FSR. (g) Experimental setups for the ATA FSR verification in anechoic chamber. Measured reflection coefficient and transmission coefficient under (h) x- and (i) y-polarized incidences. Note "A" stands for "Absorptivity" and "T" stands for "Transmittivity".

2.2. Design and Analysis of TA FSR Meta-Atom Based on k-Dispersion Control and Energy Distribution

Figure 5(a) illustrates the dispersion relations of SSPP metallic blade arrays with different lengths l_4 and the slow wave characteristics of the SSPP arrays with wave vectors larger than light ones. It is worth noting that the cut-off frequency of SSPP transmission decreases with the increase of blade array length. Therefore, in our designed SSPP metallic blade array with varying lengths l_4, the final cut-off frequency of the whole SSPP array is determined by the longest l_4. In other words, in the frequency band below the cut-off frequency determined by length l_4, the energy efficiently propagates through the metal blade array with SSPP mode, while for the high-frequency band above cut-off frequency, the energy is reflected back at different positions in the SSPP array. The higher the frequency is, the closer the reflection position is to the upper structure, because an upper shorter metal blade corresponds to a higher cutting frequency. To absorb high-frequency reflected energy, an FR4 dielectric substrate ($\varepsilon_r = 4.3$, $\tan\delta = 0.5$) with a thickness of 0.5 mm is used to support the SSPP array and generate the high dielectric loss. More importantly, the absorption effect is determined by the equation $P_a = 1/2(2\pi f\varepsilon'' + \sigma)|E|^2$, indicating that material substrates with a high imaginary part of permittivity ε'' and conductivity σ or strong electric fields E at high frequency f have stronger absorption performance P_a [53]. Strong E strength can be obtained at the cut-off frequency of SSPP array, thus resulting in perfect absorption in the high frequency band. The EM responses of the designed TA FSR with different dispersion gradient SSPP arrays are studied, plotted in Fig. 5(b). The transmission cut-off frequencies of FSR with the longest blade array length l_4 equaling to 5.2 and 6 mm are approximately 18 and 16 GHz, respectively, which are consistent with the dispersion relations in Fig. 5(a). To replace the air gap of the AT FSR mentioned above and narrow the transition band, a TA SSPP FSR with $l_4 = 5.2$ mm and $h_2 = 12$ mm is designed, exhibiting a nearly transparent window below 18 GHz and an absorption band from 19.8 to 26 GHz. In addition, Figs. 5(c)–(h) show the power loss density and power flow of SSPP arrays at 10, 21, and 24 GHz, respectively. It can be observed that EM energy can flow through the SSPP array without loss at 10 GHz. However, at 21 and 24 GHz, energy flow is blocked at different positions because power consumption occurs on the SSPP array. The higher the

TABLE 1. Comparison between the designed FSR and other works.

Ref.	Type	Transmission band (FBW), IL	Absorption band (FBW), absorptivity		Polarization	Periodicity ($@f_L$)
			lower	upper		
[17]	AT	5.1–7.2 GHz (34.1%), 1 dB	1.7–4.5 GHz (90.3%), 90%	N.A.	dual	$0.08\lambda_L$
[21]	TA	8 GHz, 2 dB	N.A.	12–26 GHz (73.7%), 75%	dual	$0.204\lambda_L$
[33]	ATA	8.1–11 GHz (30.3%), 1 dB	3.7–7.3 GHz (65.5%), 80%	12.3–14.2 GHz (14.3%), 80%	dual	$0.154\lambda_L$
[35]	ATA	7.8–11.8 GHz (40.5%), 1 dB	3.7–6.8 GHz (59%), 80%	13.7–15.3 GHz (11%), 80%	dual	$0.32\lambda_L$
[37]	ATA	1.8–2.7 GHz (40%), 3 dB	0.9–2.4 GHz (90.9%), 80%	2.8–3.3 GHz (16.4%), 80%	dual	$0.073\lambda_L$
[38]	ATA	2.8–3.8 GHz (30.3%), 3 dB	1.2–2.3 GHz (62.9%), 90%	4.2–6.9 GHz (48.6%), 90%	dual	$0.11\lambda_L$
[54]	ATA	10 GHz, 0.26 dB	3.18–9.05 GHz (96%), 90%	11.85–21.2 GHz (57%), 90%	dual	$0.12\lambda_L$
[55]	ATA	6.44–7.49 GHz (15.1%), 3 dB	1.53–6.15 GHz (120.3%), 90%	7.73–12.03 GHz (43.5%), 90%	dual	$0.11\lambda_L$
[56]	ATA	4.3 GHz, 0.81 dB	1.81–3.69 GHz (68.4%), 80%	4.95–7.43 GHz (40%), 80%	dual	$0.087\lambda_L$
This work	AT	7.8–16.9 GHz (73.7%), 1 dB	2.3–6.4 GHz (94.3%), 85%	N.A.	dual	N.A.
This work	TA	0–18 GHz (200%), 1 dB	N.A.	19.8–26 GHz (27.1%), 85%	dual	N.A.
This work	ATA	8.9–16.4 GHz (59.3%), 1 dB	2.2–6.4 GHz (97.7%), 85%	17.6–26 GHz (38.5%), 85%	dual	$0.135\lambda_L$

FBW: Fractional Bandwidth, IL: Insertion Loss, λ_L: free-space wavelength at the lowest operating frequency.

frequency is, the closer it appears to the shorter metallic blade. All results are consistent with each other, demonstrating the excellent performance of TA SSPP FSR.

2.3. Design and Performance of the Complete Multi-Characteristic ATA FSR

With the AT resistive FSR and TA SSPP FSR, we finally construct the complete ATA FSR by inserting the TA SSPP FSR into the air gap of the AT FSR. Fig. 6 depicts the whole model structure and simulated EM response of the ATA FSR meta-atom. The simulated result indicates that an ultra-wide inter-absorption band transparent window with 1 dB insertion loss ranges from 8.8 to 16.7 GHz, with a bandwidth of 62%. Moreover, two 85% absorption bands on both sides are 2.1–6.6 GHz (103.4%) and 17.2–26 GHz (36.9%), respectively. The simulated EM results of the complete ATA FSR show good consistency with the corresponding results of AT FSR and TA FSR. To qualitatively verify the bandpass-like transmission filtering characteristic of the designed ATA FSR, the simulated transmissive $\mathrm{Re}(E_x)$ field distributions of the FSR are shown in Figs. 7(a)–(c). In the low absorption band with $f_L = 2.5$ GHz, 4 GHz, and 6 GHz, and high absorption band with $f_H = 20$ GHz, 22.5 GHz, and 25 GHz, almost no EM waves can pass through the FSR, while in the middle transmission band with $f_M = 8.7$ GHz, 12 GHz, and 16.7 GHz, nearly perfect transmission phenomena can be observed. Furthermore, the simulated normalized RCS of the ATA FSR is adopted to quantitatively validate its low-scattering characteristic in both absorption and transmission bands, as delivered in Fig. 8. Consequently, compared with the same size metal plate, a significant RCS reduction exceeding 10 dB can be observed. In this way, the perfect absorption in both low and high bands, and efficient transmission in the middle band are demonstrated, in good agreement with theory and ECM analysis.

3. EXPERIMENTAL VERIFICATION

To verify our analysis and design, we manufactured an ATA FSR sample with a total area of $360 \times 360\,\mathrm{mm}^2$, including a 15×15 AT resistive sheet, a 30×30 TA SSPP array, and a 30×30 bandpass FSS, and measured it in an anechoic chamber, as depicted in Fig. 9. In the experiment, two ultra-wideband double-ridged horns have been placed on the same/different sides of ATA FSR as transmitter and receiver, respectively, to measure reflection/transmission coefficients. The transmitter

and receiver are connected to a vector network analyzer (Agilent E8362C PNA) for signal control and data processing. For reflection coefficient, a metal plate with the same size as the FSR has been employed to calibrate the reflection results of the FSR. At the same time, the measured transmission coefficient of the FSR is normalized based on the results when no samples are placed between two horns. Especially, a time-domain gating method is adopted to reduce the multipath and other environmental interference during the experiment. Figs. 9(h) and (i) show the measured reflection and transmission coefficients of the FSR under x- and y-polarized incidences, respectively. It can be observed that for both x- and y-polarized incident waves, the efficient (1 dB insertion loss) transmission characteristic ranges from 8.9 to 16.4 GHz, with two strong (85% absorptivity) absorption effects covering 2.2–6.4 GHz and 17.6–26 GHz. The good agreement between the experiment and simulation demonstrates the feasibility of the design and analysis of dual-polarized ultra-wide ATA FSR. Furthermore, the performance comparison between the designed novel FSR and other reported ones is presented in Table 1. Our FSR has significant advantage in operating bandwidth, exhibiting the widest transmission band among all reported FSRs and having two broad absorption bands. Moreover, the designed ATA FSR can be decomposed into independent AT FSR and TA FSR, both of which have better performance than other FSRs.

4. CONCLUSION

In summary, to enable a multi-characteristic ATA FSR with ultra-wideband transmission performance between two wide absorption bands, new design technique and strategy have been proposed. The novel ATA FSR consists of two independent subsets, AT FSR and TA FSR. The AT FSR is composed of a top lumped-resistor-loaded resistive sheet and a bottom four-layer cascaded ultra-wide FSS, separated by an air gap. The middle planar periodic SSPP array is equivalent to TA FSR, and the complete ATA FSR can be implemented by replacing the air gap in the AT FSR with TA FSR. After thoroughly analyzing the FSR operating mechanism based on ECM and dispersion control engineering, the transmission and scattering behaviors of the designed dual-polarized ATA FSR are further demonstrated both numerically and experimentally. Results show that the proposed FSR has a -1 dB passband from 8.9 to 16.4 GHz with a relative bandwidth of 59.3%, which is currently the widest among all reported FSRs, as well as two 85% absorption bands from 2.2 to 6.4 GHz (97.7%) and 17.6 to 26 GHz (38.5%). With the excellent performance and innovative design strategies, our FSR is quite promising in broadband stealth, shielding and compatible systems.

ACKNOWLEDGEMENT

National Natural Science Foundation of China (62371467, 62101599); Postdoctoral Innovation Talents Support Program of China (BX20190293); China Postdoctoral Science Foundation (2020M671720).

REFERENCES

[1] Yuan, J., X. Kong, K. Chen, X. Shen, Q. Wang, and C. Wu, "Intelligent radome design with multilayer composites to realize asymmetric transmission of electromagnetic waves and energy isolation," *IEEE Antennas and Wireless Propagation Letters*, Vol. 19, No. 9, 1511–1515, 2020.

[2] Bakshi, S. C., D. Mitra, and F. L. Teixeira, "FSS-based fully reconfigurable rasorber with enhanced absorption bandwidth and simplified bias network," *IEEE Transactions on Antennas and Propagation*, Vol. 68, No. 11, 7370–7381, 2020.

[3] Pang, Y., Y. Li, B. Qu, M. Yan, J. Wang, S. Qu, and Z. Xu, "Wideband RCS reduction metasurface with a transmission window," *IEEE Transactions on Antennas and Propagation*, Vol. 68, No. 10, 7079–7087, 2020.

[4] Yu, S., N. Kou, Z. Ding, and Z. Zhang, "Harmonic-absorption frequency selective rasorber based on non-resonant FSS and resistive-sheet," *IEEE Transactions on Microwave Theory and Techniques*, Vol. 69, No. 8, 3737–3745, 2021.

[5] Wang, D., Y. Zhuang, L. Shen, X. Meng, G. Wang, S. Tang, and T. Cai, "Stealth radome with an ultra-broad transparent window and a high selectivity transition band," *Optics Express*, Vol. 30, No. 10, 16 009–16 019, 2022.

[6] Sima, B., K. Chen, N. Zhang, J. Zhao, T. Jiang, and Y. Feng, "Wideband low reflection backward scattering with an interband transparent window by phase tailoring of a frequency-selective metasurface," *Journal of Physics D: Applied Physics*, Vol. 55, No. 1, 015106, 2021.

[7] Wang, Y., Y. Yuan, G. Yang, X. Ding, Q. Wu, Y. Jiang, S. N. Burokur, and K. Zhang, "Perfect control of diffraction patterns with phase-gradient metasurfaces," *ACS Applied Materials & Interfaces*, Vol. 14, No. 14, 16 856–16 865, 2022.

[8] Chen, J., W. Li, Y. Zhang, W. Ma, W. Tang, and T. Cui, "Absorption-transmission-type multifunctional coding metasurface," *Journal of Physics D: Applied Physics*, Vol. 55, No. 40, 405003, 2022.

[9] Wang, Z., G. Wang, X. Cui, and H. Bai, "Hybrid metasurface-based broadband high gain stealth antenna," *Optics Express*, Vol. 30, No. 18, 32 833–32 846, 2022.

[10] Wu, L., S. Zhong, J. Huang, and T. Liu, "Broadband frequency-selective rasorber with varactor-tunable interabsorption band transmission window," *IEEE Transactions on Antennas and Propagation*, Vol. 67, No. 9, 6039–6050, 2019.

[11] Guo, M., T. Guo, Q. Cheng, Y. Zheng, and Y. Fu, "Frequency selective rasorber with anisotropic transmission band," *IEEE Antennas and Wireless Propagation Letters*, Vol. 20, No. 2, 155–159, 2021.

[12] Wang, L., S. Liu, X. Kong, Q. Yu, X. Zhang, and H. Zhang, "A multifunctional hybrid frequency-selective rasorber with a high-efficiency cross-polarized passband/co-polarized specular reflection band," *IEEE Transactions on Antennas and Propagation*, Vol. 70, No. 9, 8173–8183, 2022.

[13] Chen, H., X.-L. Peng, X.-Z. Bo, M.-Y. Geng, X.-L. Yang, J.-L. Zhan, Z.-G. Liu, Y.-Q. Dai, and W.-B. Lu, "All-fabric flexible frequency-selective-rasorber based on cutting-transfer patterning method," *Advanced Materials Interfaces*, Vol. 9, No. 23, 2200651, 2022.

[14] Xue, K. and H. Zhai, "A compact ultrawideband frequency selective rasorber with hybrid 2-D and 3-D structure," *IEEE Antennas and Wireless Propagation Letters*, Vol. 21, No. 9, 1872–1876, 2022.

[15] Ma, Z., C. Jiang, J. Li, and X. Huang, "A dual-transmission-bands rasorber with improved absorption and oblique incidence

performance," *Scientific Reports*, Vol. 12, No. 1, 20599, 2022.
[16] Yu, D., Y. Dong, Z. Zhang, M. Lin, and L. Han, "High-selectivity frequency-selective rasorber with tunable absorptivity," *IEEE Transactions on Antennas and Propagation*, Vol. 71, No. 4, 3620–3630, 2023.
[17] Wang, Z., J. Fu, Q. Zeng, M. Song, and T. A. Denidni, "Wideband transmissive frequency-selective absorber," *IEEE Antennas and Wireless Propagation Letters*, Vol. 18, No. 7, 1443–1447, 2019.
[18] Dai, Y., Y. Fu, S. Chen, J. Wu, S. Liu, Z. Shen, and H. Yang, "Miniaturized frequency selective rasorber with absorption in S-C band and transmission in X band," *Physica Scripta*, Vol. 98, No. 2, 025506, 2023.
[19] Li, M., C. Huang, C. Huang, Y. Song, H. Shao, and J. Dong, "Graphene integrated rasorber at terahertz frequencies with functionalities of both absorption and transmission," *Results in Physics*, Vol. 41, 105959, 2022.
[20] Shen, Z., N. Kou, S. Yu, Z. Ding, and Z. Zhang, "Miniaturized frequency selective rasorber based on meander-lines loaded lumped resistors and a coupled resonator spatial filter," *Progress In Electromagnetics Research M*, Vol. 90, 147–155, 2020.
[21] Yu, S., N. Kou, Z. Ding, and Z. Zhang, "Harmonic-suppressed frequency selective rasorber using resistive-film sheet and square-loops resonator," *IEEE Antennas and Wireless Propagation Letters*, Vol. 19, No. 2, 292–296, 2020.
[22] Lin, C.-W., C.-K. Shen, and T.-L. Wu, "Ultracompact via-based absorptive frequency-selective surface for 5-GHz Wi-Fi with passbands and high-performance stability," *IEEE Transactions on Components, Packaging and Manufacturing Technology*, Vol. 8, No. 1, 41–49, 2018.
[23] Shah, G., Q. Cao, Z. A. Dayo, and M. Azeem, "Double layer multifunction frequency selective surface equipped with a tricharacteristic response," *IEEE Transactions on Electromagnetic Compatibility*, Vol. 64, No. 2, 295–302, 2022.
[24] Jia, Y., Y. Wang, J. Yin, C. Guo, H. Zhai, and C. Liu, "Design of a hybrid frequency selective rasorber with wideband reflection suppression," *IEEE Antennas and Wireless Propagation Letters*, Vol. 22, No. 2, 293–297, 2023.
[25] Ye, H., J. Wei, L. Lin, F. Liu, L. Miao, S. Bie, and J. Jiang, "A frequency-selective surface rasorber based on four functional layers," *IEEE Transactions on Antennas and Propagation*, Vol. 69, No. 5, 2768–2778, 2021.
[26] Mao, Z., K. Xu, X. Qian, and X. Chu, "A global-local design method for wideband absorption/transmission sandwich rasorber with frequency-selective surfaces," *Composite Structures*, Vol. 322, 117401, 2023.
[27] Rao, T., S. Yu, R. Shi, and N. Kou, "A dielectric matching layer loaded frequency selective rasorber with enhanced angular stabilities," *IEEE Antennas and Wireless Propagation Letters*, Vol. 22, No. 7, 1552–1556, 2023.
[28] Huang, H., C. Hua, and Z. Shen, "Absorptive frequency-selective transmission structures based on hybrid FSS and absorber," *IEEE Transactions on Antennas and Propagation*, Vol. 70, No. 7, 5606–5613, 2022.
[29] Ye, H., W. Dai, X. Chen, H. Zhang, S. Bie, and J. Jiang, "High-selectivity frequency-selective rasorber based on low-profile bandpass filter," *IEEE Antennas and Wireless Propagation Letters*, Vol. 20, No. 2, 150–154, 2021.
[30] Guo, M., D. Sang, F. Yuan, T. Guo, Y. Zheng, Q. Chen, and Y. Fu, "Broadband absorptive frequency-selective rasorber based on multilayer resistive sheets using multilayer resonator," *IEEE Transactions on Antennas and Propagation*, Vol. 70, No. 3, 2009–2022, 2022.
[31] Yang, Y., B. Wu, B. Chen, and Y. Zhao, "Flexible frequency-selective rasorber based on metal-graphene hybrid metamaterial," *Optics Express*, Vol. 30, No. 5, 6566–6576, 2022.
[32] Chen, Q., D. Sang, M. Guo, and Y. Fu, "Miniaturized frequency-selective rasorber with a wide transmission band using circular spiral resonator," *IEEE Transactions on Antennas and Propagation*, Vol. 67, No. 2, 1045–1052, 2019.
[33] Wang, L., S. Liu, X. Kong, H. Zhang, Q. Yu, and Y. Wen, "Frequency-selective rasorber with a wide high-transmission passband based on multiple coplanar parallel resonances," *IEEE Antennas and Wireless Propagation Letters*, Vol. 19, No. 2, 337–340, 2020.
[34] Xing, Q., W. Wu, Y. Yan, X. Zhang, and N. Yuan, "A wideband frequency-selective rasorber with rectangular spiral resonators," *IEEE Antennas and Wireless Propagation Letters*, Vol. 21, No. 8, 1688–1692, 2022.
[35] Yang, Z., W. Jiang, Q. Huang, and T. Hong, "A 2.5-D miniaturized frequency-selective rasorber with a wide high-transmission passband," *IEEE Antennas and Wireless Propagation Letters*, Vol. 20, No. 7, 1140–1144, 2021.
[36] Zhu, S., Z. Cao, H. Zhou, R. Geng, G. Deng, and X. Quan, "Ultra-wide transmission band frequency-selective rasorber using 2.5-D miniaturized structures," *Optics Express*, Vol. 30, No. 19, 33 980–33 993, 2022.
[37] Shen, Z., J. Wang, and B. Li, "3-D frequency selective rasorber: Concept, analysis, and design," *IEEE Transactions on Microwave Theory and Techniques*, Vol. 64, No. 10, 3087–3096, 2016.
[38] Yu, Y., G. Q. Luo, A. A. Omar, X. Liu, W. Yu, Z. C. Hao, and Z. Shen, "3D absorptive frequency-selective reflection and transmission structures with dual absorption bands," *IEEE Access*, Vol. 6, 72 880–72 888, 2018.
[39] Zhong, S., J. Feng, Z.-W. Zheng, and Y. Ma, "Ultrathin and simple 3-D rasorber based on ferrites with embedded epsilon-near-zero waveguides," *IEEE Antennas and Wireless Propagation Letters*, Vol. 21, No. 9, 1896–1900, 2022.
[40] Kianinejad, A., Z. N. Chen, and C.-W. Qiu, "Design and modeling of spoof surface plasmon modes-based microwave slow-wave transmission line," *IEEE Transactions on Microwave Theory and Techniques*, Vol. 63, No. 6, 1817–1825, 2015.
[41] Wang, C., Y. Li, M. Feng, J. Wang, H. Ma, J. Zhang, and S. Qu, "Frequency-selective structure with transmission and scattering deflection based on spoof surface plasmon polariton modes," *IEEE Transactions on Antennas and Propagation*, Vol. 67, No. 10, 6508–6514, 2019.
[42] Zhang, D., Y. Sun, K. Zhang, Q. Wu, and T. Jiang, "Short-circuited stub-loaded spoof surface plasmon polariton transmission lines with flexibly controllable lower out-of-band rejections," *Optics Letters*, Vol. 46, No. 17, 4354–4357, 2021.
[43] Zhu, Z., Y. Li, J. Zhang, J. Wang, W. Wan, L. Zheng, M. Feng, H. Chen, and S. Qu, "Absorptive frequency selective surface with two alternately switchable transmission/reflection bands," *Optics Express*, Vol. 29, No. 3, 4219–4229, 2021.
[44] Wang, D., K. Liu, X. Li, G. Wang, S. Tang, and T. Cai, "Bi-functional spoof surface plasmon polariton meta-coupler using anisotropic transmissive metasurface," *Nanophotonics*, Vol. 11, No. 6, 1177–1185, 2022.
[45] Liu, Y., K.-D. Xu, J. Li, Y.-J. Guo, A. Zhang, and Q. Chen, "Millimeter-wave E-plane waveguide bandpass filters based on spoof surface plasmon polaritons," *IEEE Transactions on Microwave Theory and Techniques*, Vol. 70, No. 10, 4399–4409, 2022.

[46] Yu, J., W. Jiang, and S. Gong, "Wideband angular stable absorber based on spoof surface plasmon polariton for RCS reduction," *IEEE Antennas and Wireless Propagation Letters*, Vol. 19, No. 7, 1058–1062, 2020.

[47] Deng, T., J. Liang, T. Cai, C. Wang, X. Wang, J. Lou, Z. Du, and D. Wang, "Ultra-thin and broadband surface wave meta-absorber," *Optics Express*, Vol. 29, No. 12, 19 193–19 201, 2021.

[48] Cheng, L., Y. Si, Z. Ji, J. Xu, J. Dong, Z. He, R. Huang, L. Zheng, L. Yan, and X. Zheng, "A novel linear gradient carbon fiber array integrated square honeycomb structure with electromagnetic wave absorption and enhanced mechanical performances," *Composite Structures*, Vol. 305, 116510, 2023.

[49] Zhang, Q., Z. Shen, J. Wang, and K. S. Lee, "Design of a switchable microwave absorber," *IEEE Antennas and Wireless Propagation Letters*, Vol. 11, 1158–1161, 2012.

[50] Langley, R. J. and E. A. Parker, "Equivalent circuit model for arrays of square loops," *Electronics Letters*, Vol. 18, No. 7, 294–296, 1982.

[51] Ferreira, D., R. F. S. Caldeirinha, I. Cuiñas, and T. R. Fernandes, "Square loop and slot frequency selective surfaces study for equivalent circuit model optimization," *IEEE Transactions on Antennas and Propagation*, Vol. 63, No. 9, 3947–3955, 2015.

[52] Ma, X., G. Wan, W. Zhang, Y. Mu, and X. Tang, "Synthesis of second-order wide-passband frequency selective surface using double-periodic structures," *IET Microwaves, Antennas & Propagation*, Vol. 13, No. 3, 373–379, 2019.

[53] Pozar, D. M., *Microwave Engineering*, 4th ed., John Wiley & Sons, New York, NY, USA, 2012.

[54] Jia, Y., Y. Wang, J. Yin, C. Guo, H. Zhai, and C. Liu, "Design of a hybrid frequency selective rasorber with wideband reflection suppression," *IEEE Antennas and Wireless Propagation Letters*, Vol. 22, No. 2, 293–297, 2023.

[55] Yu, W., M. Cheng, Y. Yu, W. Wang, L. Liu, and G. Q. Luo, "Bandpass absorptive frequency-selective structures with wide absorption bands based on hybrid 2-D and 3-D structures," *IEEE Transactions on Antennas and Propagation*, Vol. 71, No. 4, 3183–3192, 2023.

[56] Malekara, A., A. Khalilzadegan, C. Ghobadi, and J. Nourinia, "Wide-angle, dual-polarized frequency selective rasorber based on the electric field coupled resonator using characteristic mode analysis," *Journal of Applied Physics*, Vol. 133, No. 16, 164504, 2023.

[57] Cai, T., S. W. Tang, B. Zheng, G. M. Wang, W. Y. Ji, C. Qian, Z. J. Wang, E. P. Li, and H. S. Chen, "Ultrawideband chromatic aberration-free meta-mirrors," *Advanced Photonics*, Vol. 3, No. 1, 016001, 2021.

[58] Cai, T., B. Zheng, J. Lou, L. Shen, Y. H. Yang, S. W. Tang, E. P. Li, C. Qian, and H. S. Chen, "Experimental realization of a superdispersion-enabled ultrabroadband terahertz cloak," *Advanced Materials*, Vol. 34, No. 38, 2205053, 2022.